Revision 2

Word count: 7299

Dose radiation effects on quartz Al and Ti center electron spin resonance signal intensity: implications for quartz provenance discrimination

Chuanyi Wei[1,2,*], Gongming Yin[1,*], Chunru Liu[1], N'dji dit Jacques Dembele[3], Lupeng Yu[2], Huajun Jiang[4], Yawei Li[5], Rujun Guo[5], Li Cheng[1], and Wenpeng Li[6]

[1]State Key Laboratory of Earthquake Dynamics, Institute of Geology, China Earthquake Administration, Beijing 100029, China

[2]Luminescence Research Laboratory, Shandong Provincial Key Laboratory of Water and Soil Conservation and Environmental Protection, School of Resource and Environmental Sciences, Linyi University, Linyi 276000, China

[3]Université des Sciences Sociales et de Gestion de Bamako, Bamako bp2575, Mali

[4]School of Education Science, Hunan First Normal University, Changsha 410205, China

[5]School of Earth Sciences, China University of Geosciences, Wuhan 430074, China

[6]Department of Ocean Science and Engineering, Southern University of Science and Technology, Shenzhen 518055, China

***Corresponding authors:** Chuanyi Wei (chuanyiwei@ies.ac.cn) and Gongming Yin (yingongming@ies.ac.cn). **Address:** Yard No.1, Hua Yan Li, Chaoyang District, Beijing, 100029, China.

Running Title: Quartz ESR-SI as an effective sediment-provenance indicator

ABSTRACT

Quartz is one of the most common rock-forming minerals and crystallizes over a wide range of temperature and pressure conditions. This diversity of quartz crystallization environments is reflected by trace-element compositional variations, which can be used to distinguish between different source sediments. Trace elements that are incorporated into the quartz lattice form corresponding paramagnetic centers (impurity centers, such as Al and Ti centers), which can be detected using the electron spin resonance (ESR) method. However, whether the quartz impurity center ESR signal intensity (quartz ESR-SI) can be used for quartz sediment provenance tracing remains uncertain. In the present study, five present-day (modern) fluvial sediments from the Songhua, Yellow, Yangtze, Huai, and Pearl rivers in China and eight ancient fluvial sand lenses from the Yichang Gravel Layer (YGL) located in the middle Yangtze River were sampled for major- and trace-element determinations by ICP–OES and ICP–MS for the purpose of provenance discrimination. A total of 1404 ESR spectra were also measured to evaluate the effect of gamma-ray dose (varying from 50 to 50,000 Gy) on quartz ESR-SI to establish the relationship between quartz element contents and quartz ESR-SIs and thereby to assess the

potential utility of quartz ESR-SI for sediment provenance analysis. Results indicate that (1) quartz collected from the different studied locations can be distinguished by element contents; (2) the quartz Al center ESR-SI increases with increasing gamma-ray dose from 50 to 50,000 Gy; (3) the quartz Ti center ESR-SI increases within a gamma-ray dose of 10,000 Gy and decreases beyond 10,000 Gy; (4) quartz Al and Ti center ESR-SIs are closely related to the contents of Al and Ti in quartz; and (5) a plot of quartz Ti center ESR-SI versus Al center ESR-SI using data for a gamma-ray dose range of 4000–7000 Gy is the best indicator of fluvial sediment provenance using the ESR method.

Keywords: source-to-sink system, provenance tracing, quartz, electron spin resonance (ESR), Al center, Ti center

INTRODUCTION

Quartz is one of the most abundant minerals in Earth's crustal and surficial systems and is widely distributed in aeolian and fluvial-lacustrine sediments. Its resistance to physical, chemical and biological weathering has enabled its use for distinguishing sediment source/provenance (Jacamon et al., 2009; Tanner et al., 2015; Yan et al., 2017; Götte, 2018; Jaeger et al., 2019). Quartz provenance indicators include $\delta^{18}O$ composition (Jackson et al., 1981; Marin-Carbonne et al., 2011; Aléon et al., 2012; Tanner et al., 2013; Yan et al., 2014), major- and trace-element contents (Rottier et al., 2017; Monnier et al., 2018; Hong et al., 2019), oxygen vacancy detected by electron spin resonance (ESR) (Sun et al., 2007, 2008, 2013; Toyoda et

al., 2016; Wei et al., 2017, 2019) and luminescence (Lü et al., 2011; Chang et al., 2019; Nian et al., 2019) methods, and infrared (IR) spectroscopic measurements (Stalder et al., 2013, 2019; Frigo et al., 2019). Previous studies have shown that trace-element contents are useful indicators of provenance (e.g., Götze et al., 1997, 2004; Cherniak et al., 2007; Jacamon et al., 2009; Larsen et al., 2009; Breiter et al., 2013; Ackerson et al., 2015; Rottier et al., 2017; Trail et al., 2017; Tailby et al., 2018), and the substitutional incorporation of trace elements Al, Ge, and Ti into the Si position of quartz has been well established (e.g., Weil, 1984, 1993). Trace elements incorporated into the quartz lattice form its corresponding paramagnetic centers (impurity centers, such as Al and Ti centers), which can be detected using ESR analysis (Götze et al., 2004). As these impurity elements reflect the geochemical and geophysical conditions of quartz crystallization, the ESR signal intensities of quartz impurity centers (hereafter referred to as "quartz ESR-SIs") can provide information concerning the concentration and distribution of the corresponding paramagnetic lattice defects, meaning that such intensities have potential use for sediment provenance tracing.

The successful and wide application of quartz ESR-SI in geological studies includes the determination of sediment age. The ESR dating method has been used to establish a variety of geological and archaeological chronologies (e.g., Ikeya, 1975; Grün, 1989; Rink, 1997; Yin et al., 2011; Duval et al., 2016; Richter et al., 2019; Voinchet et al., 2019; Wei et al., 2020a). Besides its widespread application to age determinations of Quaternary depositional systems, quartz ESR-SIs have

84 recently been assessed for tracing sediment provenance (e.g., Sun et al., 2007, 2008,
85 2013; Tissoux et al., 2015; Toyoda et al., 2016; Saito et al., 2017; Wei et al., 2017,
86 2019, 2020b). Commonly observed paramagnetic defects in quartz include the E_1',
87 Al, and Ti centers. The heat-treated E_1' center, which refers to the E_1' center after
88 gamma-ray irradiation to more than 2000 Gy followed by heating at 300 °C for 15
89 min (Toyoda et al., 2016), is one of the most useful ESR signals for sediment
90 provenance tracing and has been successfully applied to tracing East Asian eolian
91 dust sources (Sun et al., 2007, 2008, 2013). The main principle of the heat-treated E_1'
92 center for ESR dating and provenance tracing is that quartz is irradiated by
93 radioactive nuclides in the natural environment, resulting in an increase in the
94 number of unpaired electrons in quartz with geological time. However, unlike the
95 heat-treated E_1' center, the application of impurity centers, such as the Al center and
96 Ti centers, has been rarely reported (Toyoda, 2016). Besides, previous studies have
97 focused only on describing the potential application of impurity centers to sediment
98 provenance tracing (Shimada et al., 2013; Tissoux et al., 2015), meaning that there is
99 a lack of knowledge regarding the change in the ESR-SI of impurity centers with
100 increasing radiation dose, which is the main methodological basis for the potential
101 use of such centers for distinguishing sediment provenance.

102 In the present study, five present-day fluvial sediment samples collected from
103 the Songhua, Yellow, Huai, Yangtze, and Pearl rivers and eight sand lens samples
104 collected from ancient fluvial sediments of the Yichang Gravel Layer (YGL), middle
105 Yangtze River Basin, China, were analyzed for quartz major- and trace-element

contents using inductively coupled plasma–mass spectrometry (ICP–MS) and inductively coupled plasma–optical emission spectrometry (ICP–OES). A total of 229 aliquots of 13 quartz samples were irradiated with various gamma-ray doses and prepared for ESR measurement. In total, 1404 ESR spectra were measured, allowing investigation of the effects of high-dose radiation on quartz ESR-SI as well as the relationship between major element contents and corresponding quartz ESR-SIs. The principal goal of the study was to investigate the potential use of impurity center ESR-SIs in quartz provenance discrimination.

STUDY AREA AND SAMPLING

Five present-day fluvial sediment samples were collected from five large rivers in China: the Songhua, Yellow, Huai, Yangtze, and Pearl rivers (Fig. 1-a and Table 1). The five rivers run through different geological blocks and bedrock, favoring the possible existence of differences in the trace-element composition of quartz (Tables 2 and 3). The five present-day fluvial samples were collected far from potential artificial pollution sources, and the sampling depth in each case was less than 5 cm from the floodplain surface.

Eight sand lens samples were collected from the YGL in the middle Yangtze River Basin, China. The YGL is a >100-m-thick continuous detrital sediment phase that can be observed at three successive sections, which (from oldest to youngest) are the Lijiayuan, Yunchi, and Shanxiyao sections (Fig. 1-b; Wei et al., 2020a). The Lijiayuan (LJY) Section is ~21 m thick, has an elevation of 69–92 m above sea level

(asl), and contains a basal sand lens of >10 m in thickness. The Yunchi (YC) Section is ~60 m thick, has an elevation of 92–152 m asl, and contains several sand lenses measuring 3–8 m in thickness. The Shanxiyao (SXY) Section is ~20 m thick, has an elevation of 152–173 m asl, and consists mainly of thick gravel layers with intercalated thin sand lenses.

The sedimentary facies and depositional sequence of the YGL are summarized in Fig. 1-b. More detailed information for the 13 samples is given in Table 1.

METHODS

ICP–MS and ICP–OES analyses

Major- and trace-element content determinations were performed at China University of Geosciences, Wuhan, China. Major-element contents were determined using an IRIS Intrepid II XSP ICP–OES instrument (Thermo Fisher Scientific, USA), and trace-element contents were determined using an 820MS ICP–MS instrument (Varian Corporation, USA). The relative errors on major- and trace-element contents are <2% and <5%, respectively. In preparation for ICP–MS and ICP–OES analyses, the 13 quartz samples were triturated to less than 32 μm with an agate mortar, following which 0.04 g quartz powder of each sample was placed into a 10 ml Teflon beaker. The Teflon beaker was sealed after the addition of 1.5 ml HF and 0.5 ml HNO_3. All sealed Teflon beakers were put into an air oven for 12 h at 180 °C. After removal and cooling, the Teflon beaker was unsealed and heated on an electric hot plate at 150 °C until the solution evaporated. Then, 1 ml HNO_3 and 1 ml H_2O were

added to the Teflon beaker, which was resealed and the solution dissolved for 12 h at 150 °C. After cooling to room temperature, the dissolved 0.04 g sample was prepared for content determinations using ICP–MS and ICP–OES. A standard sample was analyzed before each of the 13 quartz samples to ensure the analytical accuracy of the measured elemental compositions. The eight sand lens samples and modern sediment samples YER-01 and YAR-01 were analyzed twice by ICP–MS and ICP–OES to evaluate replicate analysis errors.

Quartz ESR measurements

Extraction of quartz. The 100–200 μm size fraction of the samples were firstly separated by wet sieving (Liu et al., 2015). All samples were then successively treated with 30% H_2O_2 and 40% HCl to remove organic material and carbonates. Magnetic minerals were removed by magnetic selection after washing and cleaning the samples with distilled water. Minerals with densities ranging between 2.57 and 2.73 g/cm^3 were separated using sodium polytungstate, following which the samples were etched using 40% HF for 40 min to remove feldspars and external irradiation by alpha particles. Fluorides created by the HF etching process were removed using HCl. Finally, all samples were rinsed in distilled water to neutralize the acid and dried at 40 °C to obtain pure quartz grains (Wei et al., 2020a).

Heating treatment. Heating treatments were performed to anneal the quartz natural ESR-SIs of the thirteen samples to zero to avoid the effect of burial time on quartz natural ESR-SI. Toyoda et al. (1991) showed that the Al center and Ti center

ESR signals are annealed to zero after heating for 15 min at about 420 °C. In the present study, all pure quartz samples were heated at 450 °C for 20 min to anneal the Al center and Ti center ESR signals. Specifically, the temperature of the muffle furnace was firstly heated to 450 °C; then the pure quartz sample was quickly put into the muffle furnace and heated at 450 °C for 20 min.

Gamma-ray dose irradiation. After the heating treatment, quartz was prepared for gamma-ray dose irradiation. Each quartz sample of the five present fluvial sediments was divided into 26 aliquots to receive gamma-ray doses of 50, 100, 200, 400, 600, 800, 1000, 1200, 1500, 1800, 2200, 2600, 3000, 3500, 4000, 4500, 5000, 6000, 7000, 8000, 9000, 10,000, 20,000, 30,000, 40,000, or 50,000 Gy to evaluate the effect of radiation dose on impurity center ESR-SI. Before applying the gamma-ray dose, each aliquot was irradiated with a 2500 Gy dose (Toyoda et al., 2016). Each quartz sample of YGL sediment was divided into 13 aliquots to receive gamma-ray doses of 100, 200, 400, 800, 1200, 1600, 2000, 2500, 3000, 5000, 6000, 7000, and 9000 Gy to further evaluate the effects of dose on the quartz impurity center ESR-SI of sediments over geological time. A total of 229 aliquots of 13 quartz samples were irradiated with ^{60}Co sources at Peking University. The dose rate was 42.25 Gy/min, calibrated by dosing of an alanine sample.

ESR measurements. In the present study, the Al and Ti centers of the possible quartz ESR impurity centers were selected for ESR analysis. ESR measurements were carried out on an X-band BRUKER EPR041XG spectrometer cooled to 77 K

with liquid nitrogen in a finger dewar at the State Key Laboratory of Earthquake Dynamics, Institute of Geology, China Earthquake Administration, Beijing, China. The Al and Ti center ESR measurements were performed using a microwave power of 5 mW and modulation amplitude of 0.16 mT. The Al center intensity was measured from the top of the peak at g = 2.018 to the bottom of the peak at g = 2.002 (Voinchet et al., 2015), whereas the Ti center intensity was measured between the top of the peak at g = 1.979 to the bottom of the peak at g = 1.913 (Fig. 2; Rink et al., 2007; Liu et al., 2010). For each impurity center, ESR signal measurements of quartz aliquots were obtained at six angles, and the mean value was calculated to reduce the variation caused by the anisotropy of quartz. Overall, 1404 signal intensity data for the Al and Ti centers were measured.

RESULTS

Major- and trace-element contents of quartz

Results of the analysis of major- and trace-element contents of the investigated quartz are summarized in Tables 2 and 3. Differences in the chemical compositions of the studied quartz samples are illustrated in Al_2O_3/TiO_2 and Al/Ti plots (Breiter et al., 2013) (Fig. 3-a and b). The Al/Ti ratio was used as a basis for investigating the discrimination of various sources of quartz (Figs. 3-c and d; Breiter et al., 2013) because the Al/Ti ratio in quartz is a good indicator of its parental melt degree (e.g., Jacamon and Larsen, 2009; Breiter et al., 2012; Ackerson et al., 2015).

Of the major elements analyzed, the contents of Al and Ti are the highest (Table

211 2). Furthermore, the investigated quartz collected from various rivers can be clearly
212 discriminated against based on the Al and Ti contents (Fig. 3-a and b). The highest
213 Al (1.5%) and Ti (0.21%) contents in quartz are found in the Pearl River sample.
214 Quartz collected from the Yangtze, Huai, Yellow, and Songhua rivers shows
215 similarly low Ti contents (~0.04%) but can be distinguished by Al content variation:
216 Songhua River (0.9%), Huai River (0.58%), Yellow River (0.35%), and Yangtze
217 River (0.13%). The quartz Al (0.04%) and Ti contents (0.02%) of the YGL have the
218 lowest values, and the contents of both of these elements are closest to those of the
219 Yangtze River (Fig. 3-a and b). Moreover, the quartz extracted from the investigated
220 five rivers can be distinguished by a plot of Na content versus Al/Ti (Fig. 3-c). For
221 Na content, the Pearl River shows the highest value (0.22%), and the Yangtze River
222 shows the lowest value (0.01%); the value for the Songhua River (0.17%) is closest
223 to that for the Pearl River, and the value for the Yellow River (0.05%) is closest to
224 that for the Yangtze River. The value for the Huai River (0.1%) is intermediate for
225 the five rivers.

226 The content of Li in quartz varies over a wide range (Fig. 3-d). The lowest
227 contents (mean 3.37 ppm) are found in the present-day fluvial sediment of the
228 Yangtze River, whereas the highest contents are recorded in the Songhua River
229 sample (5.54 ppm). The Yellow and Huai rivers show lower values (between 3.54
230 and 3.68 ppm) than those of the Pearl River (4.14 ppm) and the YGL (3.72–4.91)
231 ppm. On the whole, the information presented in Fig. 3 and Tables 2 and 3 confirms
232 that the quartz extracted from the five studied river sediments can be distinguished

by major- and trace-element contents.

ESR signal intensity

Effect of radiation dose on quartz Al center ESR-SI. The response of Al center ESR-SIs of the investigated quartz to increasing gamma-ray dose is presented in Fig. 4. Fig. 4-a and b reveal that the Al center ESR-SIs of all five present-day fluvial sediment samples increase with increasing gamma-ray dose. The Al center ESR-SIs increase markedly with increasing gamma-ray dose for doses of up to 50,000 Gy. The quartz Al center ESR-SI of the YGL samples also increases with increasing gamma-ray dose (Fig. 4-c). Quartz Al center ESR-SIs for the YGL samples are not saturated, and rather exhibit marked increases with increasing radiation dose. Fig. 4-a and b also show that the Pearl River sample exhibits the highest Al center ESR-SIs. Samples from the other four rivers display similar low Al center ESR-SIs for the same gamma-ray dose.

Effect of radiation dose on quartz Ti center ESR-SI. The response of the Ti center ESR-SIs of the investigated quartz to increasing gamma-ray dose is shown in Fig. 5. Fig. 5-a and c reveal that quartz Ti center ESR-SIs of the five present-day fluvial sediments and eight ancient fluvial sediments increase with increasing gamma-ray dose up to 10,000 Gy and 7000 Gy, respectively. Ti center ESR-SIs decrease with increasing gamma-ray dose from 10,000 to 50,000 Gy (Fig. 5-b), in contrast to the pattern for Al center ESR-SIs (Fig. 4-b). Fig. 5-c shows that quartz samples LJY-01, LJY-02, SXY-01, YC-01, and YC-03 exhibit decreasing Ti center

ESR-SI with increasing gamma-ray dose from 7000 to10,000 Gy. Fig. 5-a and b also reveal that the Pearl River sample exhibits the highest Ti center ESR-SI for the same gamma-ray dose, the Songhua and Yangtze river sediment samples show intermediate Ti center ESR-SIs, and the Yellow and Huai rivers display the lowest Ti center ESR-SIs for the same gamma-ray dose.

Al center to Ti center ESR-SI ratios. The variation in Al center to Ti center ESR-SI ratio (hereafter referred to as the quartz Al/Ti ESR-SIR) with increasing gamma-ray dose can be divided into five phases (Fig. 6-a and b):

Phase 1: Quartz Al/Ti ESR-SIRs decrease markedly at a gamma-ray dose of 2600 Gy;

Phase 2: Quartz Al/Ti ESR-SIRs show a gentle decrease for increasing gamma-ray dose from 2600 to 4000 Gy;

Phase 3: Quartz Al/Ti ESR-SIRs are essentially invariant for increasing gamma-ray dose from 4000 to 10,000 Gy;

Phase 4: Quartz Al/Ti ESR-SIRs gradually increase with increasing gamma-ray dose from 10,000 to 30,000 Gy; and

Phase 5: Quartz Al/Ti ESR-SIRs increase sharply above a gamma-ray dose of 30,000 Gy.

Quartz Al/Ti ESR-SIRs of the YGL samples decrease up to a gamma-ray dose of ~2000 Gy, above which a plateau state exists to ~7000 Gy, and an increase with

increasing gamma-ray dose above ~7000 Gy (Fig. 6-c), as in phases 1, 2, and 3 of Fig. 6-a. Nevertheless, the quartz Al/Ti ESR-SIRs of the YGL sediments are not as well defined as those of the studied present-day fluvial sediments.

DISCUSSION

Quartz ESR-SI and its relationship to element abundance

Results of the ESR measurements reveal that elements Al and Ti are incorporated into the structure of quartz (Figs. 3, 4, and 5). Al and Ti contents of the Pearl River sample are much higher than those from the Yangtze, Huai, Yellow, and Songhua rivers (Fig. 3-a and b). In addition, the quartz Al center and Ti center ESR-SIs of the Pearl River sample are much higher than those of samples collected from the Yangtze, Huai, Yellow, and Songhua rivers (Figs. 4 and 5). Titanium center and Al center ESR-SIs are higher for samples in which Ti and Al contents of quartz are higher, respectively (Figs. 3-a and 5). However, Al center ESR-SIs are not correlated with Al content, possibly because all Al contents of quartz samples were measured by ICP–OES but not all Al center signals were measured by ESR owing to the non-saturation of Al center ESR-SIs in this study. In addition, the gamma-ray dose may have been too low to transform the trace-element defects from the nonparamagnetic precursor state into paramagnetic centers (Götze et al., 2004). In conclusion, Figs. 3, 4, and 5 reveal that the measured quartz Ti center and Al center ESR-SIs are closely related to the given gamma-ray dose and that the measured quartz Ti center and Al center ESR-SIs are also closely related to the contents of Ti

295 and Al in quartz, respectively, confirming the conclusions of Usami et al. (2009) and
296 Toyoda et al. (2016).

297 **Quartz Al/Ti ESR-SIR as an effective provenance indicator**

298 On the whole, the use of quartz ESR centers as indicators of sediment
299 provenance relies on the stability of the quartz ESR measurement after the long
300 erosion–transportation–deposition cycle from source to sink (Wei et al., 2020b). The
301 results presented in Fig. 6 show that the quartz Al/Ti ESR-SIR is stable for
302 gamma-ray doses in the range of ~4000 to ~7000 Gy, which demonstrates that this
303 ratio can serve as an effective indicator of sediment provenance. This conclusion
304 appears to be sound, given that quartz Al/Ti ESR-SIRs of all five rivers presented in
305 this study showed a similar plateau pattern regardless of the fact that the rivers run
306 through different geological bodies and source rocks. The plateau value should
307 represent diagnostic information regarding source rocks (Figs. 3–6).

308 **Implications for sediment provenance tracing**

309 The ability of an indicator to distinguish among samples is an important
310 requirement for the use of quartz ESR centers as sediment provenance indicators. Fig.
311 7 shows a plot of quartz Ti center ESR-SI versus Al center ESR-SI coded by location
312 for all studied samples. The Pearl River and YGL samples display the highest Al and
313 Ti center ESR-SIs, occupying the upper-right of Fig. 7, and the Yellow and Huai
314 rivers show the lowest Al and Ti center ESR-SIs, plotting in the lower-left of Fig. 7.
315 The Yangtze and Songhua rivers exhibit intermediate Al and Ti center ESR-SIs in the

316 center of Fig. 7. It is noted that each river occupies a distinct region in Fig. 7.
317 Consequently, a plot of quartz Ti center ESR-SI vs. Al center ESR-SI with the same
318 gamma-ray dose in the range 4000–7000 Gy could be used as an effective indicator
319 of sediment provenance.

320 **IMPLICATIONS**

321 Five present-day fluvial sediment samples from the Songhua, Yellow, Huai,
322 Yangtze, and Pearl rivers in China and eight samples from the Yichang Gravel Layer
323 in the middle Yangtze River Basin were collected for determination of quartz major-
324 and trace-element contents as well analysis of quartz Al center and Ti center ESR-SIs
325 with high-dose gamma-ray dose. The study aimed to evaluate whether Al center and
326 Ti center ESR-SIs could be used as indicators of sediment provenance.

327 Results showed that the different sources of the sampled fluvial quartz could be
328 distinguished by element contents. Quartz Ti center and Al center ESR-SIs are
329 closely positively related to the content of Ti and Al in quartz, respectively. Results
330 also revealed that quartz samples from different sources could be differentiated by
331 the combined use of quartz Al center and Ti center ESR-SIs in a gamma-ray dose
332 range from 4000 to 7000 Gy. Specifically, a plot of quartz Ti center ESR-SI versus
333 Al center ESR-SI is an efficient indicator of provenance for fluvial sediments.

334 **ACKNOWLEDGMENTS**

335 This work was supported by grants from the National Natural Science
336 Foundation of China (Nos. 42002203 and 41772185), Shandong Provincial Key

337 Laboratory of Water and Soil Conservation and Environmental Protection (Grant No.
338 STKF201931), and the National Nonprofit Fundamental Research Grant of China,
339 Institute of Geology, China, Earthquake Administration (Grant Nos. IGCEA1715
340 and IGCEA2015).

341 **REFERENCES CITED**

342 Aléon, J., Chaussidon, M., Marty, B., Schütz, L., and Jaenicke, R. (2002). Oxygen
343 isotopes in single micrometer-sized quartz grains: tracing the source of Saharan
344 dust over long-distance atmospheric transport. Geochimica et Cosmochimica
345 Acta, 66, 3351-3365.

346 Breiter, K., Ackerman, L., Svojtka, M., and Müller, A. (2013). Behavior of trace
347 elements in quartz from plutons of different geochemical signature: A case
348 study from the Bohemian Massif, Czech Republic. Lithos, 175, 54-67.

349 Chang, Z., and Zhou, L. (2019). Evidence for provenance change in deep sea
350 sediments of the Bengal Fan: a 7 million year record from IODP U1444A.
351 Journal of Asian Earth Sciences, 186, 104008.

352 Cherniak, D. J., Watson, E. B., and Wark, D. A. (2007). Ti diffusion in quartz.
353 Chemical Geology, 236, 65-74.

354 Duval, M., Arnold, L. J., Guilarte, V., Demuro, M., Santonja, M., and
355 Pérez-González, A. (2017). Electron spin resonance dating of optically bleached
356 quartz grains from the Middle Palaeolithic site of Cuesta de la Bajada (Spain)

using the multiple centres approach. Quaternary Geochronology, 37, 82-96.

Frigo, C., Stalder, R., and Ludwig, T. (2019). OH defects in coesite and stishovite during ultrahigh-pressure metamorphism of continental crust. Physics and Chemistry of Minerals, 46, 77-89.

Götte, T. (2018). Trace element composition of authigenic quartz in sandstones and its correlation with fluid–rock interaction during diagenesis. Geological Society, London, Special Publications, 435, 373-387.

Goetze, J., and Ploetze, M. (1997). Investigation of trace-element distribution in detrital quartz by Electron Paramagnetic Resonance (EPR). European Journal of Mineralogy, 529-538.

Götze, J., Plötze, M., Graupner, T., Hallbauer, D. K., and Bray, C. J. (2004). Trace element incorporation into quartz: a combined study by ICP-MS, electron spin resonance, cathodoluminescence, capillary ion analysis, and gas chromatography. Geochimica et Cosmochimica Acta, 68, 3741-3759.

Grün, R. (1989). ESR dating for the early Earth. Nature, 338, 543-544.

Hong, W., Cooke, D. R., Zhang, L., Fox, N., and Thompson, J. (2019). Cathodoluminescence features, trace elements, and oxygen isotopes of quartz in unidirectional solidification textures from the Sn-mineralized Heemskirk Granite, western Tasmania. American Mineralogist, 104, 100-117.

Ikeya, M. (1975). Dating a stalactite by electron paramagnetic resonance. Nature,

255, 48-50.

Jacamon, F., and Larsen, R. B. (2009). Trace element evolution of quartz in the charnockitic Kleivan granite, SW-Norway: The Ge/Ti ratio of quartz as an index of igneous differentiation. Lithos, 107, 281-291.

Jackson, M. L. (1981). Oxygen isotopic ratios in quartz as an indicator of provenance of dust. Geol. Soc. Am. Spec. Pap., 186, 27-36.

Jaeger, D., Stalder, R., Masago, H., and Strasser, M. (2019). OH defects in quartz as a provenance tool: Application to fluvial and deep marine sediments from SW Japan. Sedimentary Geology, 388, 66-80.

Larsen, R. B., Jacamon, F., and Kronz, A. (2009). Trace element chemistry and textures of quartz during the magmatic hydrothermal transition of Oslo Rift granites. Mineralogical Magazine, 73, 691-707.

Liu, C. R., Yin, G. M., Gao, L., Bahain, J. J., Li, J. P., Lin, M., and Chen, S. M. (2010). ESR dating of Pleistocene archaeological localities of the Nihewan Basin, North China–Preliminary results. Quaternary Geochronology, 5, 385-390.

Liu, C. R., Yin, G. M., and Han, F. (2015). Effects of grain size on quartz ESR dating of Ti–Li center in fluvial and lacustrine sediments. Quaternary Geochronology, 30, 513-518.

Lü, T., and Sun, J. (2011). Luminescence sensitivities of quartz grains from eolian

deposits in northern China and their implications for provenance. Quaternary Research, 76, 181-189.

Marin-Carbonne, J., Chaussidon, M., Boiron, M. C., and Robert, F. (2011). A combined in situ oxygen, silicon isotopic and fluid inclusion study of a chert sample from Onverwacht Group (3.35 Ga, South Africa): new constraints on fluid circulation. Chemical Geology, 286, 59-71.

Monnier, L., Lach, P., Salvi, S., Melleton, J., Bailly, L., Beziat, D., ... and Gouy, S. (2018). Quartz trace-element composition by LA-ICP-MS as proxy for granite differentiation, hydrothermal episodes, and related mineralization: The Beauvoir Granite (Echassières district), France. Lithos, 320, 355-377.

Nian, X., Zhang, W., Qiu, F., Qin, J., Wang, Z., Sun, Q., ... and Liu, N. (2019). Luminescence characteristics of quartz from Holocene delta deposits of the Yangtze River and their provenance implications. Quaternary Geochronology, 49, 131-137.

Richter, M., Tsukamoto, S., and Long, H. (2019). ESR dating of Chinese loess using the quartz Ti centre: A comparison with independent age control. Quaternary International.

Rink, W. J., Bartoll, J., Schwarcz, H. P., Shane, P., and Bar-Yosef, O. (2007). Testing the reliability of ESR dating of optically exposed buried quartz sediments. Radiation Measurements, 42, 1618-1626.

417 Rink, W. J., Schwarcz, H. P., Lee, H. K., Valdés, V. C., De Quiros, F. B., and Hoyos,
418 M. (1997). ESR dating of Mousterian levels at El Castillo cave, Cantabria,
419 Spain. Journal of Archaeological Science, 24, 593-600.

420 Rottier, B., Rezeau, H., Casanova, V., Kouzmanov, K., Moritz, R., Schlöglova, K., ...
421 and Fontboté, L. (2017). Trace element diffusion and incorporation in quartz
422 during heating experiments. Contributions to Mineralogy and Petrology, 172,
423 23.

424 Saito, K., Tada, R., Zheng, H., Irino, T., Luo, C., He, M., ... and Suzuki, Y. (2017).
425 ESR signal intensity of quartz in the fine-silt fraction of riverbed sediments
426 from the Yangtze River: a provenance tracer for suspended particulate matter.
427 Progress in Earth and Planetary Science, 4, 4.

428 Shimada, A., Takada, M., and Toyoda, S. (2013). Characteristics of ESR signals and
429 TLCLs of quartz included in various source rocks and sediments in Japan: a
430 clue to sediment provenance. Geochronometria, 40, 334-340.

431 Stalder, R., and Neuser, R. D. (2013). OH-defects in detrital quartz grains: Potential
432 for application as tool for provenance analysis and overview over crustal
433 average. Sedimentary Geology, 294, 118-126.

434 Stalder, R. (2014). OH-defect content in detrital quartz grains as an archive for
435 crystallisation conditions. Sedimentary Geology, 307, 1-6.

436 Stalder, R., Potrafke, A., Billström, K., Skogby, H., Meinhold, G., Gögele, C., and

437 Berberich, T. (2017). OH defects in quartz as monitor for igneous, metamorphic,
438 and sedimentary processes. American Mineralogist, 102, 1832-1842.

439 Stalder, R., von Eynatten, H., Costamoling, J., Potrafke, A., Dunkl, I., and Meinhold,
440 G. (2019). OH in detrital quartz grains as tool for provenance analysis: Case
441 studies on various settings from Cambrian to Recent. Sedimentary geology, 389,
442 121-126.

443 Sun, Y. B., Chen, H.Z., Tada, R., Weiss, D., Lin, M., Toyoda, S., and Isozaki, Y.
444 (2013). ESR signal intensity and crystallinity of quartz from Gobi and sandy
445 deserts in East Asia and implication for tracing Asian dust provenance.
446 Geochemistry, Geophysics, Geosystems, 14, 2615-2627.

447 Sun, Y. B., Tada, R., Chen, J., Chen, H. Z., Toyoda, S. and Tani, A. (2007).
448 Distinguishing the Sources of Asian Dust Based on Electron Spin Resonance
449 Signal Intensity and Crystallinity of Quartz. Atmospheric Environment, 41,
450 8537-8548.

451 Sun, Y., Tada, R., Chen, J., Liu, Q., Toyoda, S., Tani, A., and Isozaki, Y. (2008).
452 Tracing the provenance of fine-grained dust deposited on the central Chinese
453 Loess Plateau. Geophysical Research Letters, 35.

454 Tailby N D, Cherniak D J, Watson E B. (2018). Al diffusion in quartz. American
455 Mineralogist, 103: 839-847.

456 Tanner, D., Henley, R. W., Mavrogenes, J. A., and Holden, P. (2013). Combining in

situ isotopic, trace element and textural analyses of quartz from four magmatic-hydrothermal ore deposits. Contributions to Mineralogy and Petrology, 166, 1119-1142.

Tanner, D., Henley, R. W., Mavrogenes, J. A., Holden, P., and Mernagh, T. P. (2015). Silica hydrate preserved with δ18O-rich quartz in high-temperature hydrothermal quartz in the high sulfidation copper-gold deposit at El Indio, Chile. Chemical Geology, 391, 90-99.

Tissoux, H., Voinchet, P., Lacquement, F., and Despriée, J. (2015). ESR as a method for the characterization of alluvial sediments. Radiation Measurements, 81, 2-8.

Toyoda, S., and Ikeya, M. (1991). Thermal stabilities of paramagnetic defect and impurity centers in quartz: Basis for ESR dating of thermal history. Geochemical Journal, 25, 437-445.

Toyoda, S., Nagashima, K., and Yamamoto, Y. (2016). ESR signals in quartz: Applications to provenance research–A review. Quaternary International, 397, 258-266.

Trail, D., Tailby, N., Wang, Y., Mark Harrison, T., and Boehnke, P. (2017). Aluminum in zircon as evidence for peraluminous and metaluminous melts from the H adean to present. Geochemistry, Geophysics, Geosystems, 18, 1580-1593.

Usami, T., Toyoda, S., Bahadur, H., Srivastava, A. K., and Nishido, H. (2009).

Characterization of the E1′ center in quartz: Role of aluminum hole centers and oxygen vacancies. Physica B: Condensed Matter, 404, 3819-3823.

Voinchet, P., Toyoda, S., Falguères, C., Hernandez, M., Tissoux, H., Moreno, D., and Bahain, J. J. (2015). Evaluation of ESR residual dose in quartz modern samples, an investigation on environmental dependence. Quaternary Geochronology, 30, 506-512.

Voinchet, P., Yin, G., Falguères, C., Liu, C., Han, F., Sun, X., and Bahain, J. J. (2019). Dating of the stepped quaternary fluvial terrace system of the Yellow River by electron spin resonance (ESR). Quaternary Geochronology, 49, 278-282.

Wei, C. Y., Liu, C. R., Li, W. P., Zhang, Z. J., Zhang, H. S., Zhao, J. X., and Zhang, L. Y. (2017). Nature ESR signals of quartz E' center shed new light on river sediments provenance: A case study in southeast margin of the Tibet Plateau. Quaternary International, 454, 38-44.

Wei, C. Y., Liu, C. R., Li, C. A., Yin, G. M., Zhang, Y. F., Li, W. P., and Yu, L. P. (2019). Application of long time artificial optical bleaching of the E1'centre to sediment ESR dating. Geochronometria, 46, 79-86.

Wei, C. Y., Voinchet, P., Zhang, Y., Bahain, J. J., Liu, C., Kang, C., and Sun, X. (2020a). Chronology and Provenance of the Yichang Gravel Layer deposits in the Jianghan Basin, Middle Yangtze River Valley, China: Implications for the Timing of Channelization of the Three Gorges Valley. Quaternary International.

497 Wei, C. Y., Liu, C. R., Yin G. M., Li W. P., (2020b). Electron spin resonance (ESR)
498 signal intensity of quartz E1 ' center and its potential use in fluvial sediments
499 provenance tracing. Geochronometria, in press.

500 Weil, J. A. (1984). A review of electron spin spectroscopy and its application to the
501 study of paramagnetic defects in crystalline quartz. Physics and Chemistry of
502 Minerals, 10, 149-165.

503 Weil, J. A. (1993). A review of the EPR spectroscopy of the point defects in α-quartz:
504 the decade 1982–1992. In The Physics and Chemistry of SiO2 and the Si-SiO2
505 Interface 2, 131-144.

506 Yan, Y., Ma, L., and Sun, Y. (2017). Tectonic and climatic controls on provenance
507 changes of fine-grained dust on the Chinese Loess Plateau since the late
508 Oligocene. Geochimica et Cosmochimica Acta, 200, 110-122.

509 Yan, Y., Sun, Y., Chen, H., and Ma, L. (2014). Oxygen isotope signatures of quartz
510 from major Asian dust sources: Implications for changes in the provenance of
511 Chinese loess. Geochimica et Cosmochimica Acta, 139, 399-410.

512 Yin, G., Bahain, J. J., Shen, G., Tissoux, H., Falguères, C., Dolo, J. M., and Shao, Q.
513 (2011). ESR/U-series study of teeth recovered from the palaeoanthropological
514 stratum of the Dali Man site (Shaanxi Province, China). Quaternary
515 Geochronology, 6, 98-105.

516

Figure captions

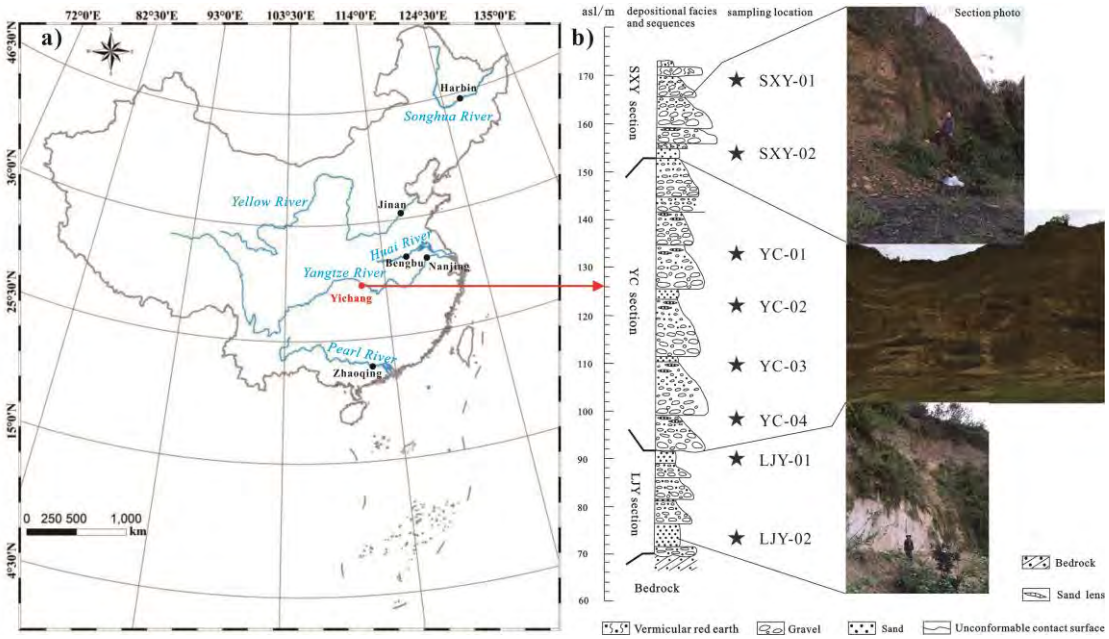

Figure 1. Sampling locations of the present study. (a) Sampling locations of the five present-day fluvial sediments and the Yichang Gravel Layer (YGL); (b) Sedimentary logs of sampling sites in the YGL, middle Yangtze River Basin, with the locations of individual samples marked.

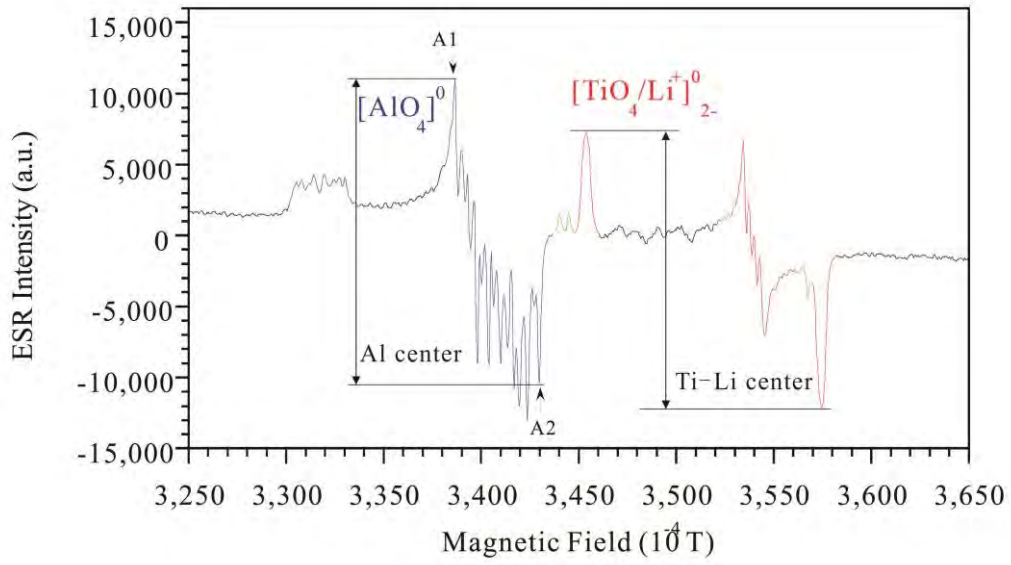

524 **Figure 2.** Typical ESR spectra of quartz Al and Ti centers.

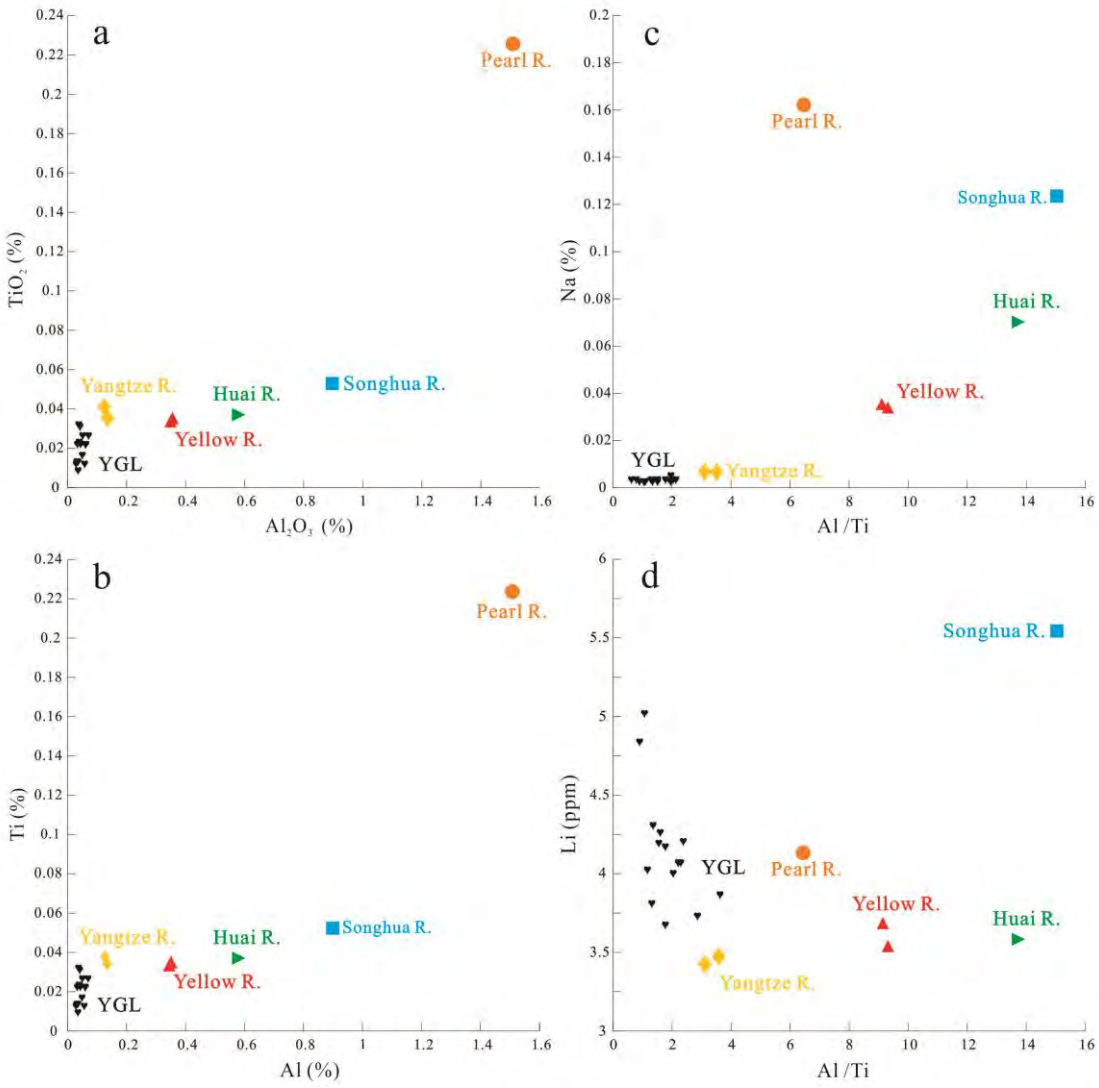

525

526 **Figure 3.** Major- and trace-element contents of the studied quartz. (a) TiO_2 vs. Al_2O_3;

527 (b) Ti vs. Al; (c) Na vs. Al/Ti; (d) Li vs. Al/Ti.

528

529

This is the peer-reviewed, final accepted version for American Mineralogist, published by the Mineralogical Society of America.
The published version is subject to change. Cite as Authors (Year) Title. American Mineralogist, in press.
DOI: https://doi.org/10.2138/am-2020-7565. http://www.minsocam.org/

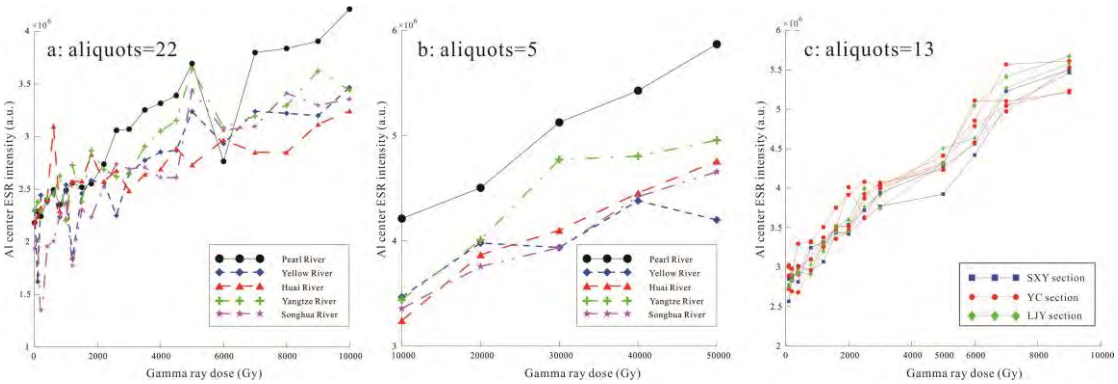

Figure 4. Response of quartz Al center ESR-SI to gamma-ray dose. (a) Variation in quartz Al center ESR-SI of five fluvial sediment samples for a gamma-ray dose of up to 10,000 Gy; (b) Variation in quartz Al center ESR-SI of five fluvial sediments for a gamma-ray dose range of 10,000 to 50,000 Gy; (c) Variation in quartz Al center ESR-SI of eight YGL sediment samples for a gamma-ray dose of up to 9000 Gy.

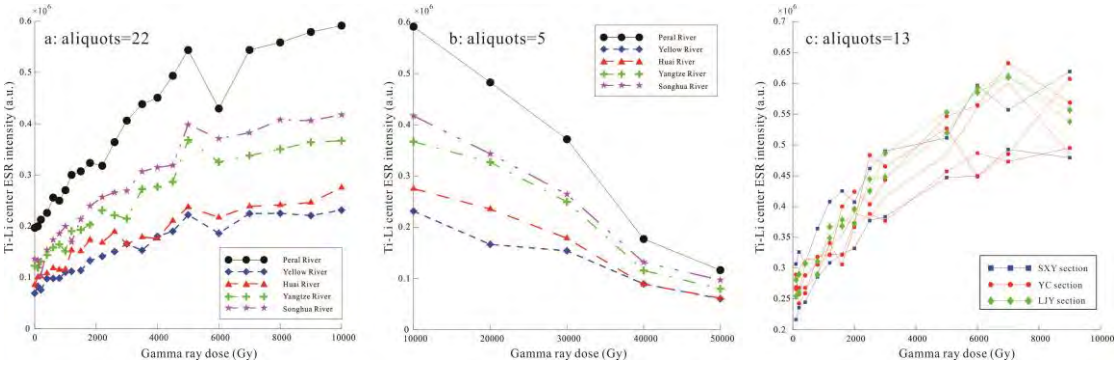

Figure 5. Response of quartz Ti center ESR-SI to gamma-ray dose. (a) Variation in quartz Ti center ESR-SI of five fluvial sediment samples for a gamma-ray dose of up to 10,000 Gy; (b) Variation in quartz Ti center ESR-SI of five fluvial sediments for a gamma-ray dose range of 10,000 to 50,000 Gy; (c) Variation in quartz Ti center ESR-SI of eight YGL sediment samples for a gamma-ray dose of up to 9000 Gy.

This is the peer-reviewed, final accepted version for American Mineralogist, published by the Mineralogical Society of America.
The published version is subject to change. Cite as Authors (Year) Title. American Mineralogist, in press.
DOI: https://doi.org/10.2138/am-2020-7565. http://www.minsocam.org/

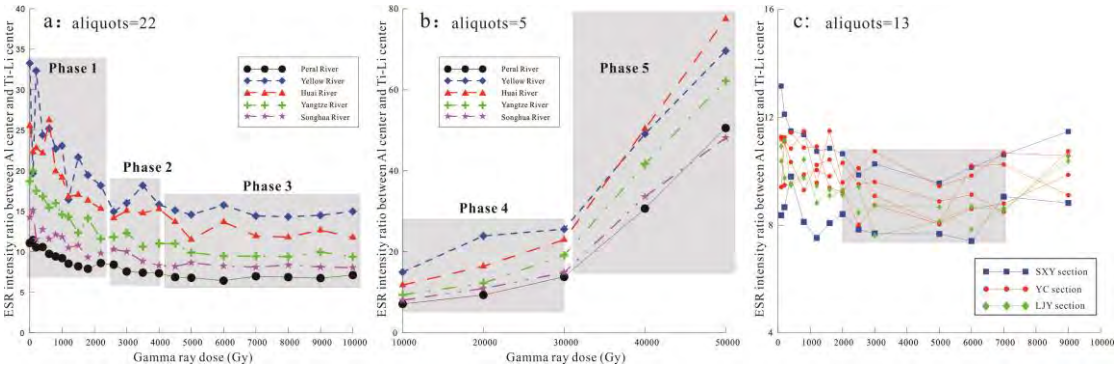

Figure 6. Variation in quartz Al center to Ti center ESR-SIR with increasing gamma-ray dose. (a) Variation in quartz ESR-SIR of five fluvial sediment samples for a gamma-ray dose of up to 10,000 Gy; (b) Variation in quartz ESR-SIR of five fluvial sediments for a gamma-ray dose range of 10,000 to 50,000 Gy; (c) Variation in quartz ESR-SIR of eight YGL sediment samples for a gamma-ray dose of up to 9000 Gy.

This is the peer-reviewed, final accepted version for American Mineralogist, published by the Mineralogical Society of America.
The published version is subject to change. Cite as Authors (Year) Title. American Mineralogist, in press.
DOI: https://doi.org/10.2138/am-2020-7565. http://www.minsocam.org/

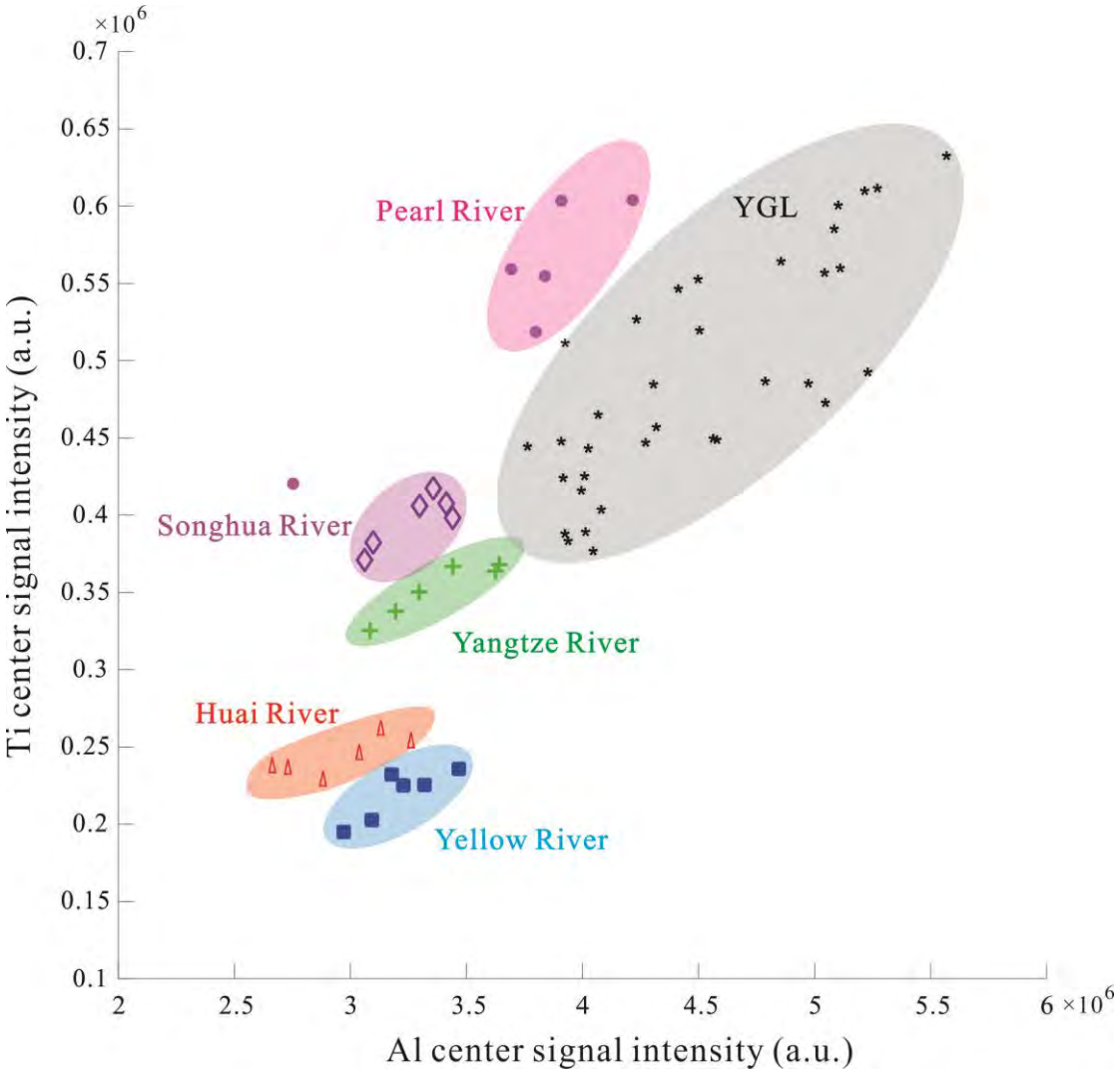

551

552 **Figure 7.** Plot of quartz Ti center ESR-SI vs. quartz Al center ESR-SI for all samples

553 investigated in the present study.

554

555

556

557

558

559 **Table 1.** Sample information for the different sampling locations of the present
560 study.

No.	Sample name	Sampling site (city)	Sampling river/section	Latitude (N)	Longitude (E)	Property
1	SHR-01	Harbin	Songhua R.	45°41′15″	126°11′04″	Present-day fluvial sediment
2	YER-01	Jinan	Yellow R.	36°43′31″	117°00′41″	
3	HR-01	Bengbu	Huai R.	32°57′12″	117°15′49″	
4	YAR-01	Nanjing	Yangtze R.	32°04′00″	118°42′24″	
5	PR-01	Zhaoqing	Pearl R.	23°04′59″	112°11′40″	
6	SXY-01	Yichang	Shanxiyao section of YGL	30°28′53″	111°27′39″	Ancient fluvial sediment
7	SXY-02					
8	YC-01		Yunchi section of YGL	30°28′52″	111°27′30″	
9	YC-02					
10	YC-03					
11	YC-04					
12	LJY-01		Lijiayuan section	30°28′23″	111°27′	

This is the peer-reviewed, final accepted version for American Mineralogist, published by the Mineralogical Society of America.
The published version is subject to change. Cite as Authors (Year) Title. American Mineralogist, in press.
DOI: https://doi.org/10.2138/am-2020-7565. http://www.minsocam.org/

13	LJY-02		of YGL		12″	

561

562 **Table 2.** Major-element contents of the investigated quartz samples, determined

563 using ICP–OES.

Sample name	Al_2O_3 (%)	CaO (%)	Fe_2O_3 (%)	K_2O (%)	MgO (%)	MnO (%)	Na_2O (%)	TiO_2 (%)
SHR-01	0.902	0.156	0.028	0.111	0.093	0.001	0.167	0.053
YER-01-a1	0.352	0.041	0.022	0.034	0.014	0.001	0.047	0.034
YER-01-a2	0.348	0.045	0.024	0.034	0.015	0.001	0.046	0.033
HR-01	0.575	0.080	0.034	0.069	0.029	0.001	0.095	0.037
YAR-01-a1	0.130	0.018	0.009	0.010	0.018	0.000	0.009	0.036
YAR-01-a2	0.134	0.021	0.011	0.010	0.018	0.000	0.009	0.034
PR-01	1.50	0.272	0.044	0.117	0.043	0.001	0.219	0.205
SXY-01-a1	0.066	0.025	0.053	0.003	0.012	0.001	0.006	0.027
SXY-01-a2	0.032	0.016	0.003	0.002	0.003	0.000	0.003	0.023
SXY-02-a1	0.048	0.031	0.026	0.002	0.013	0.001	0.004	0.027
SXY-02-a2	0.042	0.028	0.016	0.003	0.009	0.001	0.003	0.023
YC-01-a1	0.036	0.017	0.003	0.002	0.003	0.000	0.004	0.032
YC-01-a2	0.040	0.012	0.006	0.003	0.005	0.000	0.004	0.031
YC-02-a1	0.037	0.021	0.014	0.002	0.005	0.001	0.003	0.024
YC-02-a2	0.038	0.017	0.013	0.002	0.005	0.001	0.003	0.024

This is the peer-reviewed, final accepted version for American Mineralogist, published by the Mineralogical Society of America.
The published version is subject to change. Cite as Authors (Year) Title. American Mineralogist, in press.
DOI: https://doi.org/10.2138/am-2020-7565. http://www.minsocam.org/

YC-03-a1	0.034	0.019	0.006	0.002	0.005	0.000	0.003	0.011
YC-03-a2	0.054	0.029	0.019	0.002	0.012	0.001	0.004	0.014
YC-04-a1	0.028	0.013	0.005	0.002	0.004	0.000	0.003	0.014
YC-04-a2	0.047	0.034	0.029	0.002	0.015	0.001	0.004	0.018
LJY-01-a1	0.030	0.016	0.004	0.002	0.005	0.000	0.004	0.015
LJY-01-a2	0.034	0.015	0.017	0.002	0.007	0.000	0.004	0.015
LJY-02-a1	0.056	0.017	0.014	0.003	0.005	0.000	0.003	0.023
LJY-02-a2	0.058	0.008	0.015	0.003	0.005	0.000	0.004	0.023

564 Note: “a1” denotes the analysis of aliquot 1, and “a2” denotes the analysis of aliquot

565 2 of the same sample.

This is the peer-reviewed, final accepted version for American Mineralogist, published by the Mineralogical Society of America.
The published version is subject to change. Cite as Authors (Year) Title. American Mineralogist, in press.
DOI: https://doi.org/10.2138/am-2020-7565. http://www.minsocam.org/

566 **Table 3.** Trace-element contents of the investigated quartz samples, determined using ICP–MS.

Element	SHR-01	YER-01-a1	YER-01-a2	HR-01	YAR-01-a1	YAR-01-a2	PR-01	SXY-01-a1	SXY-01-a2	SXY-02-a1	SXY-02-a2	YC-01-a1	YC-01-a2	YC-02-a1	YC-02-a2	YC-03-a1	YC-03-a2	YC-04-a1	YC-04-a2	LJY-01-a1	LJY-01-a2	LJY-02-a1	LJY-02-a2
Li	5.54	3.68	3.54	3.58	3.27	3.47	4.14	4.07	4.03	4.18	4.24	4.75	4.91	3.84	4.28	3.77	3.89	3.72	4.19	4.16	4.01	4.07	4.07
Be	0.240	0.095	0.102	0.657	0.067	0.059	0.172	0.029	0.033	0.041	0.030	0.039	0.036	0.033	0.034	0.036	0.031	0.027	0.028	0.035	0.029	0.049	0.039
B	2.45	1.11	1.08	0.939	2.51	1.61	2.82	1.21	0.899	1.54	5.02	1.38	1.10	1.92	1.11	0.587	0.260	0.406	1.39	1.14	1.52	1.08	1.52
Sc	0.294	0.210	0.240	0.372	0.355	0.178	0.513	1.66	1.31	1.51	1.53	1.04	1.45	1.49	1.48	1.40	1.17	1.78	0.983	1.18	1.24	1.40	1.42
V	1.3	0.918	0.806	1.1	0.765	0.923	6.9	0.749	0.891	0.764	0.792	0.48	0.58	0.80	0.72	0.47	0.39	0.46	0.61	0.39	0.32	0.71	0.62

	5			4			4					9	5	5	2	4	4	4	0	4	7	0	6
Cr	0.798	1.07	1.62	1.39	1.38	2.58	6.13	0.185	0.158	0.811	0.883	0.673	0.247	7.49	6.94	1.03	0.855	0.112	0.171	0.377	0.371	0.312	1.33
Co	0.050	0.049	0.047	0.063	0.038	0.061	0.078	0.099	0.058	0.078	0.076	0.064	0.075	0.141	0.303	0.060	0.058	0.035	0.053	0.036	0.059	0.055	0.061
Ni	0.050	0.011	0.026	0.024	0.16	0.164	0.132	<0.05	<0.05	<0.05	<0.05	<0.05	<0.05	<0.05	<0.05	<0.05	<0.05	<0.05	<0.05	<0.05	<0.05	<0.05	<0.05
Cu	0.859	0.746	0.694	0.886	1.18	1.18	1.10	0.645	0.732	0.783	1.00	0.844	0.682	1.45	1.91	1.85	0.955	1.15	0.763	0.739	1.68	1.14	1.09
Zn	0.452	3.04	2.40	1.36	0.736	2.52	3.29	4.07	4.01	1.50	2.74	3.37	4.01	1.88	2.53	3.73	4.42	11.3	8.53	40.7	38.0	55.6	56.6
Ga	0.990	0.438	0.431	0.644	0.192	0.215	2.18	0.047	0.078	0.053	0.058	0.057	0.054	0.053	0.050	0.043	0.048	0.035	0.047	0.044	0.042	0.082	0.079

This is the peer-reviewed, final accepted version for American Mineralogist, published by the Mineralogical Society of America.
The published version is subject to change. Cite as Authors (Year) Title. American Mineralogist, in press.
DOI: https://doi.org/10.2138/am-2020-7565. http://www.minsocam.org/

Ge	0.248	0.210	0.220	0.231	0.219	0.221	0.232	0.253	0.255	0.247	0.229	0.239	0.248	0.250	0.235	0.218	0.245	0.233	0.230	0.218	0.243	0.225	0.231
Rb	3.73	1.55	1.45	2.20	0.651	0.575	2.81	0.120	0.060	0.080	0.026	0.043	0.121	0.044	0.065	0.082	0.004	0.124	0.127	<0.05	0.007	0.160	0.122
Sr	22.7	8.65	8.59	15.1	2.53	2.92	37.9	1.08	1.39	2.14	0.849	0.491	0.605	0.865	1.31	0.855	0.743	0.026	1.12	0.148	0.612	0.864	1.09
Y	1.62	1.42	1.44	1.67	1.65	1.63	3.73	1.09	0.922	0.927	0.930	1.45	1.30	1.00	1.15	0.942	0.614	0.611	0.883	0.803	0.734	1.48	0.997
Zr	84.7	198	208	120	294	270	310	13.8	12.7	21.2	23.1	23.8	26.5	16.7	23.5	10.1	9.12	13.7	16.0	14.5	19.2	23.3	17.0
Nb	1.35	0.699	0.636	0.812	0.685	0.648	4.25	0.389	0.389	0.345	0.341	0.562	0.545	0.398	0.367	0.169	0.154	0.234	0.269	0.277	0.288	0.487	0.517
Cd	0.0	0.009	0.004	0.0	0.010	0.003	0.0	0.006	0.006	0.013	0.017	0.01	0.00	0.01	0.02	0.01	0.00	0.00	0.00	0.00	0.04	0.00	0.00

	15			08			20					3	8	1	0	3	5	4	9	6	2	9	8
Cs	0.092	0.054	0.053	0.075	0.033	0.037	0.067	0.032	0.034	0.038	0.031	0.033	0.033	0.030	0.033	0.029	0.030	0.031	0.028	0.029	0.029	0.059	0.066
Ba	56.1	26.8	26.7	39.3	12.9	23.2	61.1	4.38	8.30	4.18	7.13	2.67	7.98	4.95	3.84	2.89	8.57	6.94	1.63	6.35	5.15	2.18	6.77
Nd	1.73	1.02	1.08	1.31	0.981	1.20	5.51	0.679	1.77	0.799	0.861	0.992	1.03	0.783	0.651	0.533	0.661	0.535	0.985	0.578	0.559	1.05	0.526
Sm	0.294	0.201	0.189	0.231	0.193	0.224	0.991	0.134	0.253	0.157	0.166	0.185	0.182	0.144	0.124	0.124	0.117	0.106	0.188	0.102	0.101	0.209	0.106
Hf	2.15	4.79	4.91	2.82	7.13	6.56	7.42	0.967	1.64	10.6	16.8	1.10	0.936	3.68	7.17	5.62	1.28	0.593	0.517	0.808	0.573	0.673	0.717
Ta	0.099	0.063	0.046	0.057	0.047	0.053	0.255	0.032	0.036	0.028	0.025	0.046	0.042	0.031	0.030	0.015	0.013	0.019	0.023	0.018	0.019	0.029	0.030

This is the peer-reviewed, final accepted version for American Mineralogist, published by the Mineralogical Society of America.
The published version is subject to change. Cite as Authors (Year) Title. American Mineralogist, in press.
DOI: https://doi.org/10.2138/am-2020-7565. http://www.minsocam.org/

Pb	1.77	0.683	0.773	1.15	0.382	18.4	1.85	0.557	0.520	0.831	0.500	0.482	0.473	0.519	0.829	0.403	0.443	0.563	0.814	0.408	0.483	0.480	0.400
Th	0.590	0.444	0.468	0.568	0.569	0.671	0.861	0.333	0.428	0.603	0.477	0.455	0.442	0.375	0.313	0.334	0.404	0.328	0.531	0.346	0.295	0.804	0.409
U	0.276	0.301	0.362	0.252	0.410	0.392	0.541	0.096	0.090	0.126	0.097	0.140	0.128	0.094	0.104	0.071	0.064	0.095	0.118	0.085	0.082	0.130	0.118

Note: “a1” denotes the analysis of aliquot 1, and “a2” denotes the analysis of aliquot 2 of the same sample.